AAAS
Research
Volume 2020, Article ID 2196063, 11 pages
https://doi.org/10.34133/2020/2196063

*Research Article*

# Construction of 1D/2D $\alpha$-$Fe_2O_3$/$SnO_2$ Hybrid Nanoarrays for Sub-ppm Acetone Detection

**Huimin Gong,[1] Changhui Zhao,[1] Gaoqiang Niu,[1] Wei Zhang,[2] and Fei Wang[1]**

[1]*School of Microelectronics, Southern University of Science and Technology, Shenzhen 518055, China*
[2]*Department of Electrical and Electronic Engineering, Southern University of Science and Technology, Shenzhen 518055, China*

Correspondence should be addressed to Changhui Zhao; zhaoch@sustech.edu.cn and Fei Wang; wangf@sustech.edu.cn

Received 24 September 2019; Accepted 19 December 2019; Published 13 February 2020



Exhaled acetone is one of the representative biomarkers for the noninvasive diagnosis of type-1 diabetes. In this work, we have applied a facile two-step chemical bath deposition method for acetone sensors based on $\alpha$-$Fe_2O_3$/$SnO_2$ hybrid nanoarrays (HNAs), where one-dimensional (1D) FeOOH nanorods are in situ grown on the prefabricated 2D $SnO_2$ nanosheets for on-chip construction of 1D/2D HNAs. After annealing in air, ultrafine $\alpha$-$Fe_2O_3$ nanorods are homogenously distributed on the surface of $SnO_2$ nanosheet arrays (NSAs). Gas sensing results show that the $\alpha$-$Fe_2O_3$/$SnO_2$ HNAs exhibit a greatly enhanced response to acetone (3.25 at 0.4 ppm) at a sub-ppm level compared with those based on pure $SnO_2$ NSAs (1.16 at 0.4 ppm) and pure $\alpha$-$Fe_2O_3$ nanorods (1.03 at 0.4 ppm), at an operating temperature of 340°C. The enhanced acetone sensing performance may be attributed to the formation of $\alpha$-$Fe_2O_3$–$SnO_2$ n-n heterostructure with 1D/2D hybrid architectures. Moreover, the $\alpha$-$Fe_2O_3$/$SnO_2$ HNAs also possess good reproducibility and selectivity toward acetone vapor, suggesting its potential application in breath acetone analysis.

## 1. Introduction

As a potential alternative for the noninvasive diagnosis of disease, exhaled breath analysis has been proposed and developed over the past decades [1–3]. The exhaled breath of human beings includes not only nitrogen, oxygen, carbon dioxide, nitric oxide, and water vapor but also a mixture of volatile organic compounds (VOCs) and some other nonvolatile molecules. Encouragingly, a few of them have been regarded as biomarkers to diagnose diseases (Table S1). For example, formaldehyde (lung cancer) [4], toluene (lung cancer) [5], ammonia (hemodialysis) [6], $H_2S$ (halitosis) [7], isoprene (heart disease) [8], benzene (smoker) [9], and pentane (acute asthma) [10] at few dozens to few thousands of ppb are known as biomarkers for patients. Researchers have also found that exhaled acetone can intuitively correlate with type-1 diabetes, which may exceed 1.8 ppm (only 0.3–0.9 ppm for healthy people) [1, 11]. Therefore, an ultrasensitive acetone sensor is of great importance to detect acetone vapor at a sub-ppm level.

Metal oxide semiconductors (MOXs), such as $SnO_2$, ZnO, $\alpha$-$Fe_2O_3$, CuO, and NiO, have been widely explored in the field of gas detection owing to their simple and cost-effective synthesis, high sensitivity, and good stability. Among these MOXs, $\alpha$-$Fe_2O_3$ is a multifunctional n-type semiconductor with a direct bandgap ($E_g$ = 2.2 eV at 300 K) that has been intensively investigated in the field of gas sensing [12–15]. Several effective strategies have been designed to improve the gas sensing properties of these MOXs, such as doping, surface modification, porous/hollow structures, and hierarchical architectures [16–18]. Recently, construction of hybrid nanostructures is rapidly emerging as a fascinating strategy that combines different MOXs with precise control of their morphologies, such as hollow ZnO/$ZnFe_2O_4$ heterostructures that were synthesized by growing ultrathin $ZnFe_2O_4$ nanosheets on the outer surface of ZnO hollow microspheres [19], NiO nanoparticle-decorated $SnO_2$ nanosheets [20], CuO nanosheets/ZnO nanorods (NRs) [21], and $Fe_2O_3$ nanoparticle-decorated CuO NRs [22]. For this purpose, the rational combination of $SnO_2$ and $\alpha$-$Fe_2O_3$ has been proven to improve their gas sensing performances (Table S2). The results show that the $\alpha$-$Fe_2O_3$/$SnO_2$ composites present excellent sensing performances to acetone [23, 24], ethanol [25–30], toluene [31], and LPG [32, 33]. Moreover, their gas sensing properties can be largely affected by the size and shape of nanobuilding blocks ($\alpha$-$Fe_2O_3$ and $SnO_2$). As far as

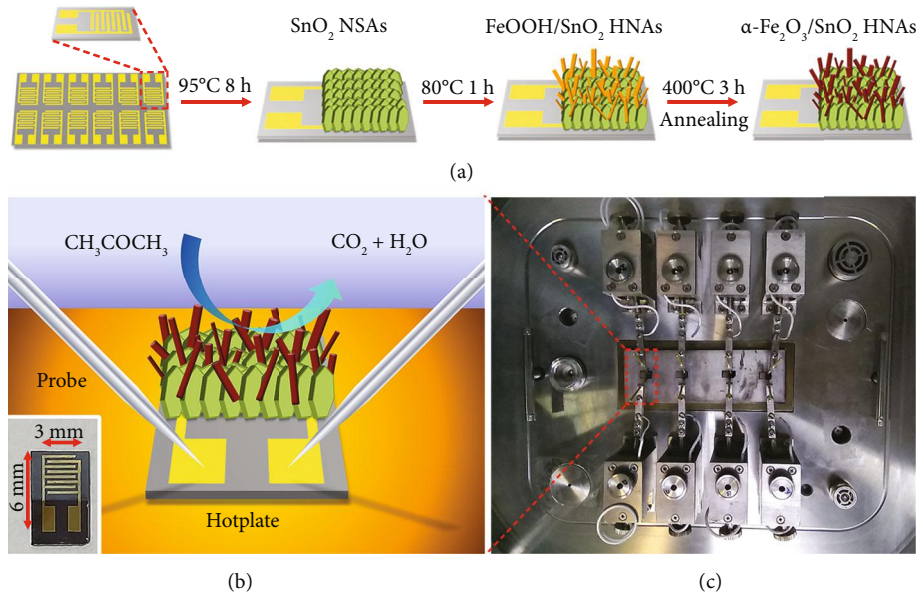


FIGURE 1: Schematic diagrams of (a) synthesis process of $\alpha$-$Fe_2O_3/SnO_2$ HNAs and (b) gas sensing measurement platform; the inset shows the digital photograph of the $\alpha$-$Fe_2O_3/SnO_2$ HNAs gas sensing chips. (c) A photograph of the test platform of CGS-4TPs.

we know, only a few reports about $\alpha$-$Fe_2O_3$–$SnO_2$ system have concerned on the detection of ultralow concentrations of acetone.

In this work, we report a two-step chemical bath deposition (CBD) method to construct the $\alpha$-$Fe_2O_3/SnO_2$ hybrid nanoarrays (HNAs) on-chips with subsequent annealing in air. The one-dimensional (1D) $\alpha$-$Fe_2O_3$ NRs are distributed homogenously on the surface of the 2D $SnO_2$ nanosheets to construct novel 1D/2D HNAs. In comparison with pure $SnO_2$ NSAs and $\alpha$-$Fe_2O_3$ NRs, the $\alpha$-$Fe_2O_3/SnO_2$ HNAs show a dramatically enhanced response to acetone (down to sub-ppm). Moreover, the $\alpha$-$Fe_2O_3/SnO_2$ HNAs also possess a superior selectivity to acetone against other interfering gases (formaldehyde, toluene, benzene, and ammonia). A possible sensing mechanism based on the formation of $\alpha$-$Fe_2O_3$–$SnO_2$ n-n heterostructure is proposed.

## 2. Results and Discussion

*2.1. Morphological Characteristics.* As illustrated in Figure 1(a), a chip with interdigital Au electrodes (200 $\mu$m lines separated by 200 $\mu$m gaps) was fabricated on a (100) silicon substrate with a 2 $\mu$m thermally grown $SiO_2$ layer, and the $SnO_2$ NSAs were prepared with an on-chip growth method similar to our previous work [34]. The chip was vertically dipped into the mixed solution (containing $Sn^{2+}$ and $CO(NH_2)_2$) during this process, and then the prefabricated $SnO_2$ NSAs were immersed in another aqueous solution (containing $Fe^{2+}$ and $CO(NH_2)_2$) for depositing FeOOH NRs on $SnO_2$ NSAs. After annealing in air, the as-prepared sensors were placed on a CGS-4TP gas sensing measurement system. A schematic of the gas sensing measurement systems used in this work is illustrated in Figure S1. Figure 1(b) presents a schematic diagram of the test platform used in this work. A hotplate was used to adjust the operating temperature, and two pins of a sensor were connected with a pair of probes. A digital photograph of the gas sensing chip (3 mm × 6 mm in size) with $\alpha$-$Fe_2O_3/SnO_2$ HNAs is given in the inset of Figure 1(b). During the test, four sensors were measured simultaneously, as shown Figure 1(c), and the electrical resistance of each sensor was recorded.

Figure 2 shows the morphologies of as-prepared pure $SnO_2$ NSAs and $\alpha$-$Fe_2O_3/SnO_2$ HNAs. It can be seen from Figure 2(a) that the pure $SnO_2$ NSAs are composed by oriented growth of nanosheets, where the adjacent $SnO_2$ nanosheets will interconnect with each other and form a semiopen network. From the cross-sectional scanning electron microscope (SEM) images of $SnO_2$ NSAs (Figure 2(b)), the flake-like $SnO_2$ stands vertically on the chip with a uniform film thickness (~100 nm), and the $SnO_2$ NSAs are robustly adhered to the substrate. After the growth of $\alpha$-$Fe_2O_3$ NRs, it is obvious that the surface morphology of $\alpha$-$Fe_2O_3/SnO_2$ HNAs is much different from that of the pure $SnO_2$ NSAs. As shown in Figure 2(c), numerous ultrathin $\alpha$-$Fe_2O_3$ NRs are homogenously distributed among the interconnected $SnO_2$ NSAs. A SEM close-up image of $\alpha$-$Fe_2O_3$ NRs (inset Figure 2(c)) reveals that the diameter of NRs ranges from 9 nm to 20 nm, and the average diameter is about 12.7 nm. Otherwise, for the second-step (CBD method), the $\alpha$-$Fe_2O_3$ NRs tend to form irregular aggregates without a substrate (Figure S2). The cross-sectional SEM images of $\alpha$-$Fe_2O_3/SnO_2$ HNAs in Figure 2(d) further indicate that the 1D $\alpha$-$Fe_2O_3$ NRs are in situ grown on the surface of 2D $SnO_2$ nanosheets, and novel 1D/2D hybrid nanoarrays can be achieved by a facile two-step CBD method. At the same time, the average film thickness of $\alpha$-$Fe_2O_3/SnO_2$ HNAs increases up to 220 nm.

To get further insight into the definite morphology of pure $SnO_2$ NSAs and $\alpha$-$Fe_2O_3/SnO_2$ HNAs, transmission electron microscope (TEM) images were taken from the

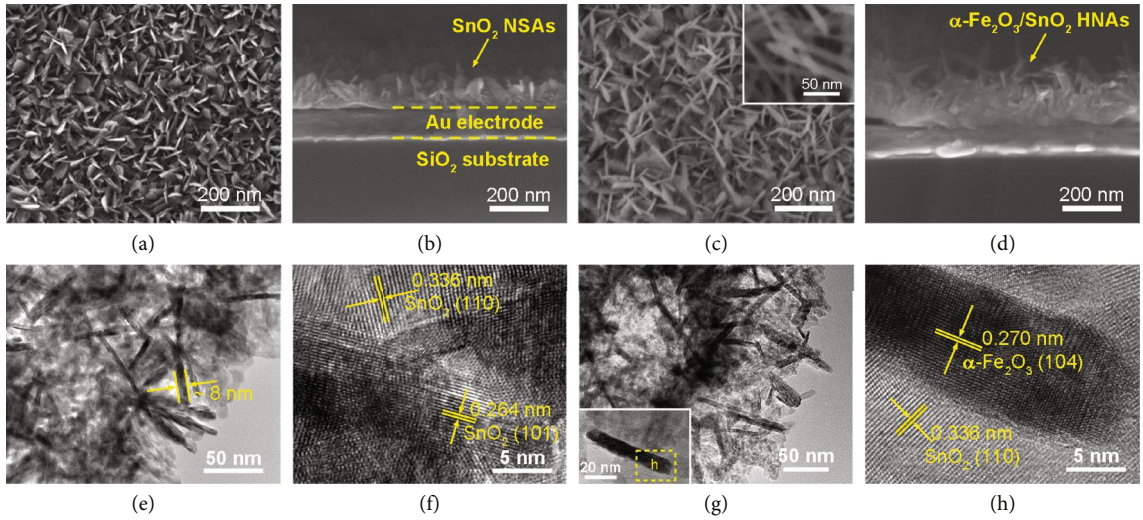


FIGURE 2: Top view SEM images of (a) $SnO_2$ NSAs and (c) $\alpha$-$Fe_2O_3$/$SnO_2$ HNAs. Cross-sectional SEM images of (b) $SnO_2$ NSAs and (d) $\alpha$-$Fe_2O_3$/$SnO_2$ HNAs. The inset of (c) shows a SEM close-up image of $\alpha$-$Fe_2O_3$ NRs. (e) TEM and (f) HRTEM images of the pure $SnO_2$ NSAs. (g) TEM and (h) HRTEM images of $\alpha$-$Fe_2O_3$/$SnO_2$ HNAs. The inset of (g) shows an individual $\alpha$-$Fe_2O_3$ rod grown on the surface of $SnO_2$ nanosheet.

scraped-off products. As shown in Figure 2(e), $SnO_2$ NSAs made up of interconnecting flakes with a thickness of <10 nm are obtained. Because of the vertical direction of growth, the thickness of a $SnO_2$ nanosheet can be easily measured in Figure 2(e) (marked by arrows, ~8 nm). These 2D nanosheets have an edge length of tens of nanometers, which agree well with the SEM observation (Figure 2(a)). A high-resolution TEM (HRTEM) image (Figure 2(f)) reveals the fringe patterns in $SnO_2$ NSAs, and the *d*-spacings of 0.264 and 0.336 nm are assigned to the interplanar distances of (101) and (110) planes of rutile $SnO_2$, respectively.

For $\alpha$-$Fe_2O_3$/$SnO_2$ HNAs, the overall TEM image (Figure 2(g)) indicates that the hybrid composites are constructed by interconnected 2D nanosheets and some disordered 1D nanorods with respect to their different structural features. The inset of Figure 2(g) shows an individual nanorod grown on the surface of the nanosheet. The diameter of the rod is around 9 nm, and the length is estimated to be 57 nm. Figure 2(h) provides the HRTEM image of the selected region from the inset of Figure 2(g) (marked by a dashed rectangle). The lattice fringes with *d*-spacings of 0.270 and 0.336 nm can be indexed to the (104) plane of $\alpha$-$Fe_2O_3$ and (110) plane of $SnO_2$, respectively. These results further confirm the construction of the 1D/2D hybrid nanostructure of $\alpha$-$Fe_2O_3$/$SnO_2$ HNAs.

The chemical composition of the samples was identified by EDS and XPS analysis. The EDS mapping and spectrum of $\alpha$-$Fe_2O_3$/$SnO_2$ HNAs are depicted in Figures 3(a)–3(c) and 3(d), respectively. Sn (Figure 3(b)) and Fe (Figure 3(c)) elements were distributed randomly and uniformly on the substrate, which was in agreement with the fact that the hybrid composites were constructed by hybrid $\alpha$-$Fe_2O_3$ and $SnO_2$. The existence of Sn and Fe elements was confirmed by the EDS characterization, and the atomic percentages of Sn and Fe were measured to be 5.38% and 4.17%, respectively.

Moreover, XPS analysis was used to obtain more information about the chemical valences of our samples. Figure 4(a) displays the high-resolution Sn 3d spectra of $SnO_2$ NSAs and $\alpha$-$Fe_2O_3$/$SnO_2$ HNAs. In the pure $SnO_2$ NSAs, the two peaks centered at 487.4 and 495.8 eV can be ascribed to the peaks of Sn $3d_{5/2}$ and Sn $3d_{3/2}$, respectively, which are in good agreement with $Sn^{4+}$. With the modification of $\alpha$-$Fe_2O_3$, a slight negative shift of the binding energies is observed in $\alpha$-$Fe_2O_3$/$SnO_2$ HNAs, shifting to 487.3 and 495.7 eV, respectively, as a result of the formation of $\alpha$-$Fe_2O_3$/$SnO_2$ heterojunction interface. In the spectrum of Fe 2p in Figure 4(b), interference peaks are detected at 717.6 eV in $SnO_2$ NSAs and 716.5 eV in $\alpha$-$Fe_2O_3$/$SnO_2$ HNAs, which come from the Sn 3p peak. The Fe 2p peaks are not found in $\alpha$-$Fe_2O_3$/$SnO_2$ HNAs due to the strong interference peak. In comparison, the two peaks at 711.9 and 725.2 eV detected in pure $\alpha$-$Fe_2O_3$ NRs are attributed to Fe $2p_{3/2}$ and Fe $2p_{1/2}$, respectively, corresponding to $Fe^{3+}$ in $\alpha$-$Fe_2O_3$.

*2.2. Gas Sensing Properties.* As is well-known, the gas sensing properties of MOXs are highly dependent on the operating temperature. To confirm it, the as-prepared gas sensors were examined at various temperatures (280-380°C) toward 5 ppm acetone. The sensor response is defined as $R_a/R_g$, where $R_a$ and $R_g$ are the sensor resistance in air and target gas, respectively. As shown in Figure 5(a), the response of $\alpha$-$Fe_2O_3$/$SnO_2$ HNA-based sensor increases with the increase in operating temperature and reaches its maximum value (13.63) at 340°C, then decreases with the further increase of operating temperature. Therefore, 340°C can be chosen as the optimum operating temperature of $\alpha$-$Fe_2O_3$/$SnO_2$ HNAs. Differently, the pure $SnO_2$ NSA-based sensor exhibits no obvious variation over the whole temperature range (2.00, at 340°C). The pure $\alpha$-$Fe_2O_3$ NR-based sensor shows a monotonic decrease of the response with an increase in operating

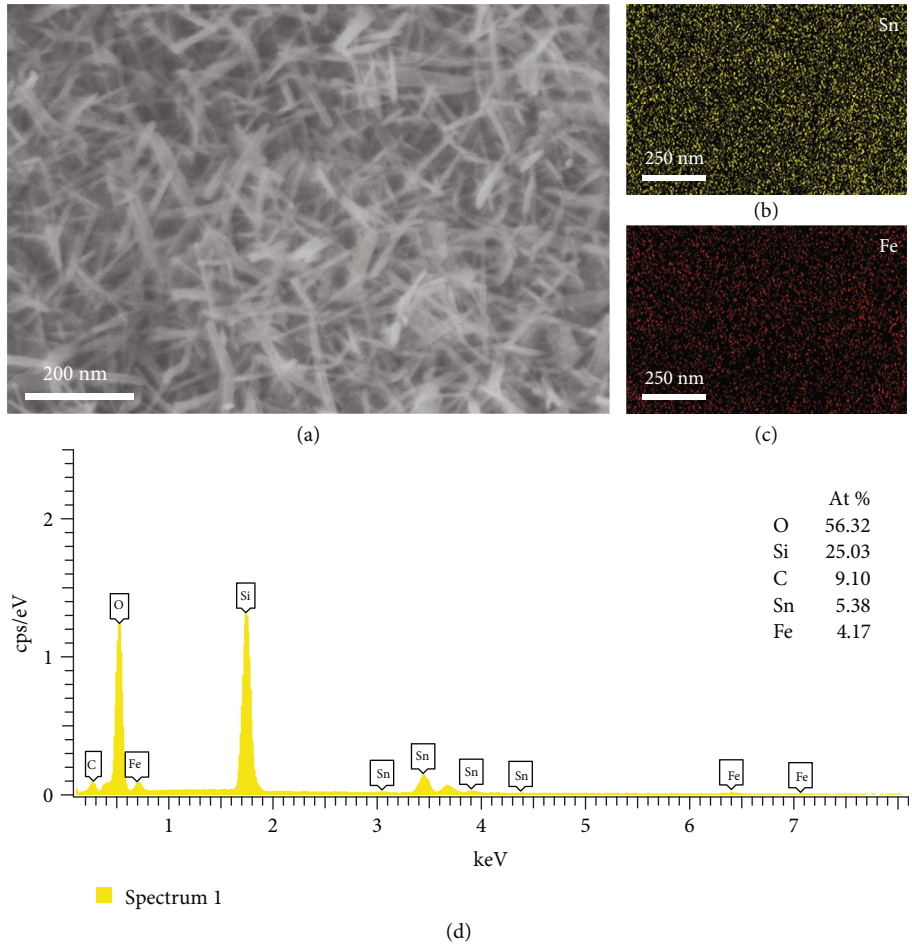


Figure 3: (a) SEM image, (b–c) the corresponding EDS mapping images, and (d) EDS spectrum of $\alpha$-$Fe_2O_3$/$SnO_2$ HNAs.

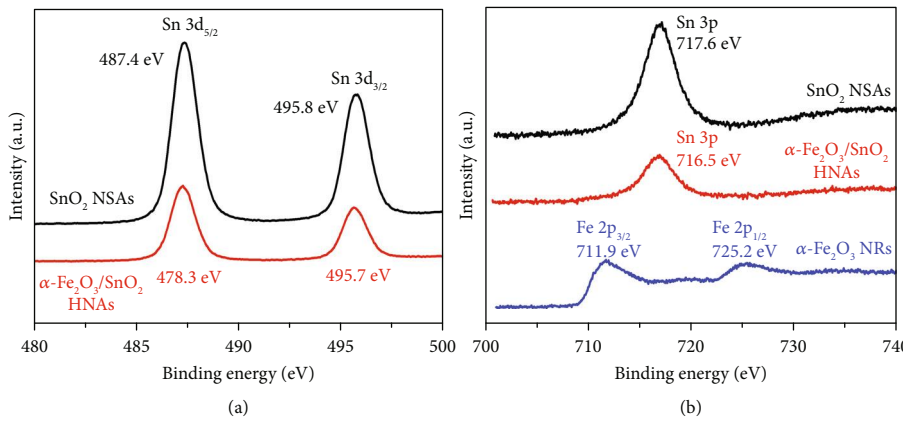


Figure 4: The high-resolution XPS spectra of $SnO_2$ NSAs, $\alpha$-$Fe_2O_3$ NRs, and $\alpha$-$Fe_2O_3$/$SnO_2$ HNAs: (a) Sn 3d and (b) Fe 2p.

temperature, and the highest response value is about 4.28 at 280°C. It is clear that the $\alpha$-$Fe_2O_3$/$SnO_2$ HNA-based sensor displays the highest response in the three sensors, revealing that the acetone sensing properties of $SnO_2$ NSAs can be significantly enhanced by the modification of $\alpha$-$Fe_2O_3$ NRs.

Figure 5(b) gives the acetone sensing properties of the above three sensors at the same operating temperature of 340°C. It is clear that the sensor response increases with the acetone concentration ranging from 0.4 to 20 ppm for each sensor. Especially, in the case of $\alpha$-$Fe_2O_3$/$SnO_2$ HNAs, the response increases rapidly over the whole concentration range, which is rather different from the other two sensors. The response values of $\alpha$-$Fe_2O_3$/$SnO_2$ HNAs are 3.25, 4.64, 5.37, 7.68, 9.91, 10.69, 12.34, 16.55, and 21.26 toward 0.4,

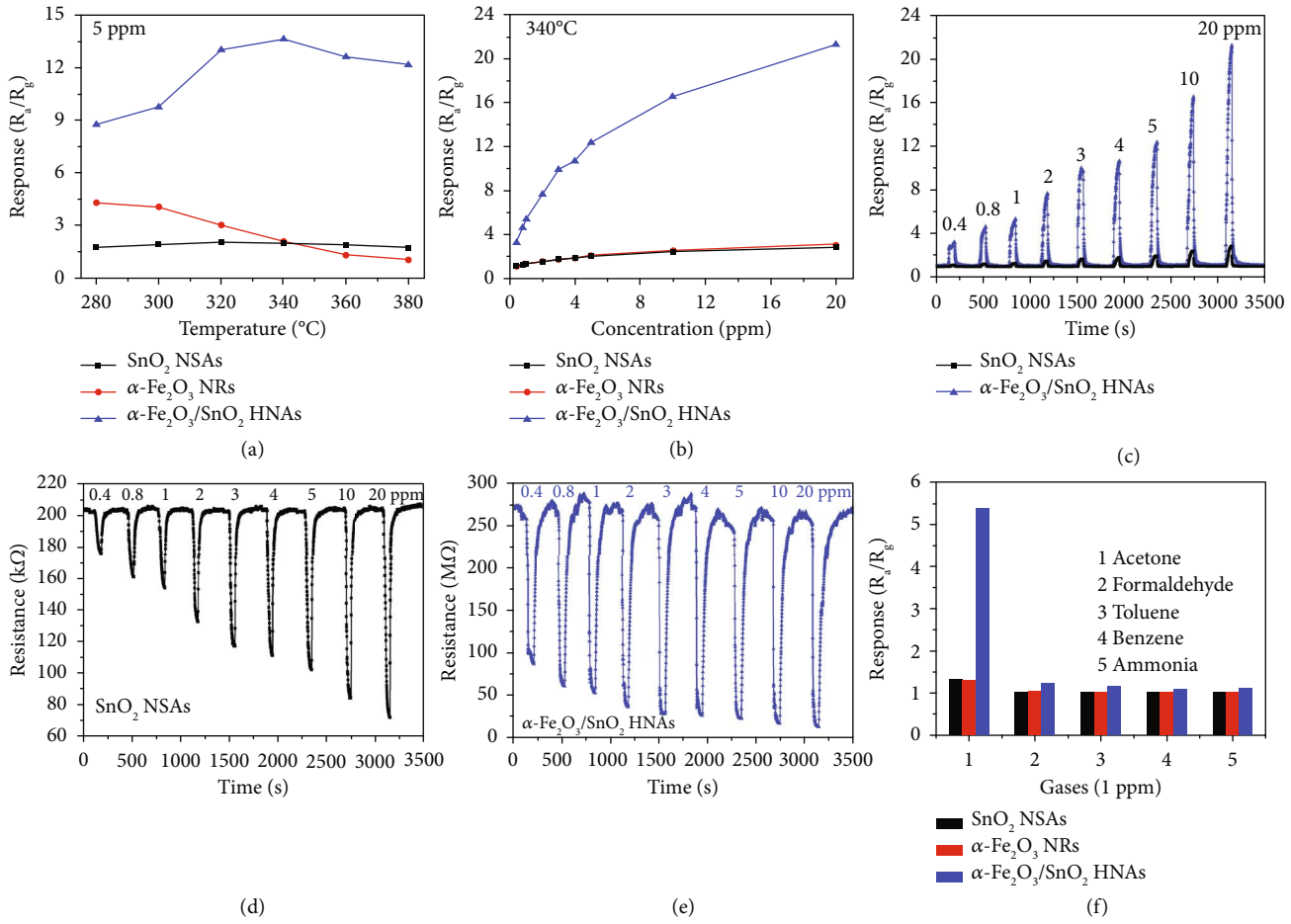


FIGURE 5: (a) Sensor responses of the pure $SnO_2$ NSAs, $\alpha$-$Fe_2O_3$ NRs, and $\alpha$-$Fe_2O_3/SnO_2$ HNAs toward 5 ppm acetone as a function of operating temperature (280-380°C). (b) Sensor responses *vs.* acetone concentration (0.4-20 ppm) at 340°C. The corresponding transient response curves of (c) $SnO_2$ NSAs and $\alpha$-$Fe_2O_3/SnO_2$ HNAs. Resistance curves of (d) $SnO_2$ NSAs and (e) $\alpha$-$Fe_2O_3/SnO_2$ HNAs at 340°C. (f) Selectivity of the sensors to various gases (1 ppm) at 340°C.

0.8, 1, 2, 3, 4, 5, 10, and 20 ppm acetone, respectively. In comparison, the response values of pure $SnO_2$ NSAs and $\alpha$-$Fe_2O_3$ NRs toward acetone can be as low as 1.16 and 1.03, respectively, at a concentration of 0.4 ppm, and their values are still less than 3.1 even toward 20 ppm acetone. Therefore, the $\alpha$-$Fe_2O_3/SnO_2$ HNA-based sensor exhibits the highest response values toward acetone in the three sensors, indicating the improvement of sensitivity.

Figure 5(c) plots the corresponding transient response curves of the pure $SnO_2$ NSA- and $\alpha$-$Fe_2O_3/SnO_2$ HNA-based sensors over an acetone concentration range of 0.4 to 20 ppm recorded at 340°C. Obviously, these response curves present a sharp increase upon acetone exposure and can recover to their original values in air. In accordance with these, the sensor resistance curves are shown in Figures 5(d) and 5(e). Amongst them, the $\alpha$-$Fe_2O_3/SnO_2$ HNA-based sensor exhibits a higher resistance in air ($R_a$, 282.683 MΩ, Figure 5(e)) than that of pure $SnO_2$ NSAs (204.05 kΩ, Figure 5(d)) and $\alpha$-$Fe_2O_3$ NRs (132.298 MΩ, Figure S3(b)). Upon exposure to acetone gas, the sensor resistance quickly decreases as expected and then recovers to its $R_a$ after being exposed to air. $R_g$ decreases monotonically with the increase of acetone concentration; in other words, the sensor response increases (refer to Figure 5(c) and Figure S3(a)).

The response and recovery times ($t_{res}$ and $t_{rec}$) are very important parameters for high-performance gas sensors. The response time $t_{res}$ (or recovery time $t_{rec}$) is defined as the time required to reach 90% resistance change when the sensor is exposed to target gas (or air). As shown in Figure S4, the $\alpha$-$Fe_2O_3/SnO_2$ HNA-based sensor shows a faster $t_{res}$ (14 s, at 1 ppm) at 340°C compared with that of the $SnO_2$ NSAs (37 s, at 1 ppm). On the contrary, the $t_{rec}$ of the $\alpha$-$Fe_2O_3/SnO_2$ HNA-based sensor always exceeds one minute (62–159 s, in the range 0.4–20 ppm), which is apparently higher than that of the $SnO_2$ NSA-based sensor (22–34 s, in the range 0.4–20 ppm). According to the previous studies, the vertically ultrathin $SnO_2$ NSAs can provide as much surface area as possible to adsorb gas molecules and facilitate the adsorption/desorption of the acetone gas. When the $\alpha$-$Fe_2O_3$ NRs were introduced, the branched $\alpha$-$Fe_2O_3$ NRs on the surface of $SnO_2$ NSAs will adsorb more acetone molecules, making the $\alpha$-$Fe_2O_3/SnO_2$ HNAs more sensitive and present faster response toward acetone.

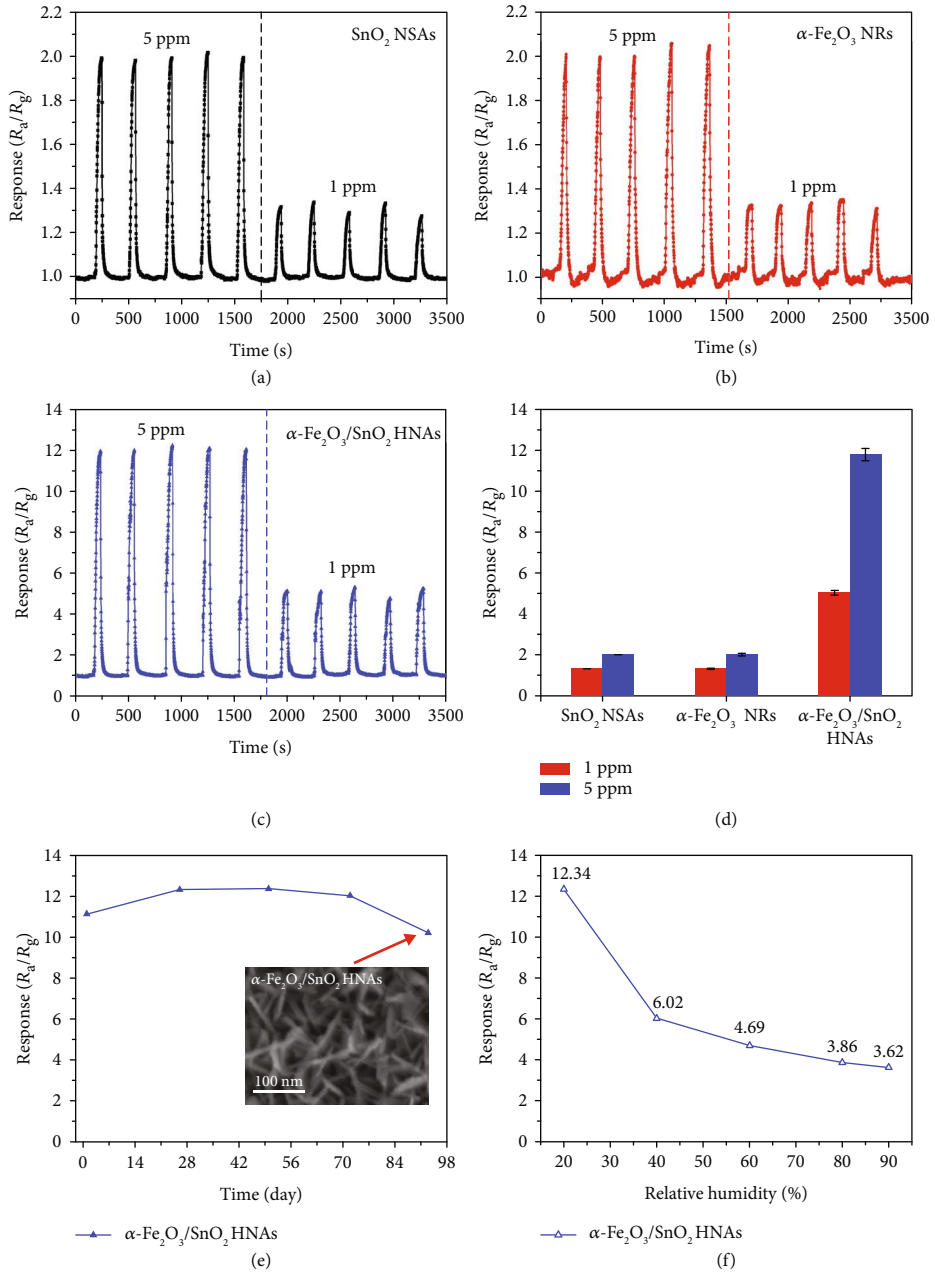


Figure 6: Reproducibility of (a) $SnO_2$ NSAs, (b) $\alpha$-$Fe_2O_3$ NRs, and (c) $\alpha$-$Fe_2O_3$/$SnO_2$ HNA-based sensors toward acetone (5 ppm and 1 ppm, each of 5 cycles) at 340°C; (d) is the corresponding comparison of the sensor responses. (e) Stability of $\alpha$-$Fe_2O_3$/$SnO_2$ HNA-based sensor toward 5 ppm acetone at 340°C for 93 days; the inset is the SEM image of $\alpha$-$Fe_2O_3$/$SnO_2$ HNAs taken after 93 days of gas sensing test. (f) Response of $\alpha$-$Fe_2O_3$/$SnO_2$ HNA-based sensor to 5 ppm acetone at 340°C under different relative humidity (20–90% RH).

To study the selectivity in the above sensors, some interfering gases (formaldehyde, toluene, benzene, and ammonia) were measured at 340°C with a low concentration of 1 ppm. It can be seen in Figure 5(f) that the $\alpha$-$Fe_2O_3$/$SnO_2$ HNA-based sensor exhibits higher responses toward all gases than those of pure $SnO_2$ NSAs and $\alpha$-$Fe_2O_3$ NRs. Especially, all the sensors obtain their highest responses toward acetone compared with other interfering gases. In the case of the $\alpha$-$Fe_2O_3$/$SnO_2$ HNA-based sensor, it shows the highest response toward acetone (5.37), then toward formaldehyde (1.23) and toluene (1.16) and is almost insensitive toward ammonia (1.11) and benzene (1.09). On the other hand, the corresponding responses of pure $SnO_2$ NSAs toward above gases are 1.33, 1.02, 1.02, 1.02, and 1.01 in turn (for $\alpha$-$Fe_2O_3$ NRs: 1.30, 1.03, 1.02, 1.03, and 1.03). These results suggest that the $\alpha$-$Fe_2O_3$ NRs, indeed, have a significant impact on the selectivity of the $SnO_2$ NSAs toward acetone.

The reproducibility of the sensors at 340°C has been investigated by continuously testing the sensors to 5 ppm and 1 ppm acetone with 5 cycles for each. As shown in Figures 6(a)–6(c), all the sensors maintain their response

Table 1: Comparison of the acetone sensing properties of MOX-based sensors.

| Materials | Temperature (°C) | RH (%) | Detection range (ppm) | Response ($R_a/R_g$) | $t_{res}/t_{rec}$ (s/s) | Ref. |
|---|---|---|---|---|---|---|
| $\alpha$-$Fe_2O_3/SnO_2$ HNAs | 340 | 20 | 0.4–20 | 5.37@1 ppm | 14/70 | This work |
| Pt-$SnO_2$ fibers | 300 | 80 | 0.12–3 | 3.47@3 ppm | 15/6 | 35 |
| ZnO@ZIF-CoZn nanowire arrays | 260 | 0–90 | 10–2000 | 2.3@10 ppm | 43/61 | 36 |
| PdO-$Co_3O_4$ hollow nanocages | 350 | 90 | 0.4–5 | 1.52*@1 ppm | — | 37 |
| NiO/ZnO hollow spheres | 275 | 30 | 0.8–100 | 1.6@0.8 ppm | 1/20 | 38 |
| ZnO/CuO inverse opals | 310 | 93.5 | 0.2–50 | 1.8@1 ppm | 7/13 | 11 |

*$R_g/R_a$.

values without obvious variation (less than 4%) during the cyclic testing, indicating excellent reproducibility of our devices. By comparison, Figure 6(d) illustrates the statistical analysis of the results of sensor responses (for $SnO_2$ NSAs sensor: $1.32 \pm 0.02$ at 1 ppm and $2.00 \pm 0.01$ at 5 ppm; $\alpha$-$Fe_2O_3$ NRs sensor: $1.33 \pm 0.03$ at 1 ppm and $2.02 \pm 0.06$ at 5 ppm; $\alpha$-$Fe_2O_3/SnO_2$ HNAs sensor: $5.05 \pm 0.11$ at 1 ppm and $11.80 \pm 0.29$ at 5 ppm), further demonstrating their robustness as acetone sensors.

To assess the long-term stability of our sensor, we tested the $\alpha$-$Fe_2O_3/SnO_2$ HNA-based sensor for 93 days toward 5 ppm acetone at 340°C. The mean response of the $\alpha$-$Fe_2O_3/SnO_2$ HNA-based sensor is 11.62 with a standard deviation estimated to be 0.93 during the whole period, suggesting its stability for acetone detection over a long period. Furthermore, it can be clearly seen that there is no obvious change between the nanostructures of $\alpha$-$Fe_2O_3/SnO_2$ HNAs before (Figure 2(c)) and after (inset of Figure 6(e)) a number of gas sensing tests. This observation is consistent with the good long-term stability of the $\alpha$-$Fe_2O_3/SnO_2$ HNA-based sensor.

It is well-known that human exhaled breath is highly humid (RH ≥ 80%) and the existence of water vapor has a significant influence on the gas sensing performance for MOX-based gas sensors. As shown in Figure 6(f), the response of $\alpha$-$Fe_2O_3$ NRs to 5 ppm acetone was measured as a function of relative humidity (20%–90% RH). The responses of $\alpha$-$Fe_2O_3/SnO_2$ HNAs under 20%, 40%, 60%, 80%, and 90% RH were 12.34, 6.02, 4.69, 3.86, and 3.62, respectively. Obviously, the response of $\alpha$-$Fe_2O_3/SnO_2$ HNAs is highly dependent on relative humidity, and some available approaches (such as employing water filtering membranes) are needed to eliminate the influence of water vapor.

Considering the previous reports in Table 1 [11, 35–38], the $\alpha$-$Fe_2O_3/SnO_2$ HNA-based sensor in this work possesses relatively medium sensitivity (or operating temperature). We can conclude that the acetone sensing properties of MOXs can be further enhanced by constructing heterostructures or modifying with noble metals. As mentioned before, the acetone detection capability (or resolution) for the diagnosis of diabetes mellitus should be as low as sub-ppm, all of which need sufficient and reliable sensors for acetone. In this sense, the high sensitivity, good selectivity, and excellent reproducibility of the $\alpha$-$Fe_2O_3/SnO_2$ HNA-based sensor imply that it can potentially be used for breath acetone analysis.

*2.3. Sensing Mechanism.* For n-type MOXs ($SnO_2$ and $\alpha$-$Fe_2O_3$), their acetone sensing mechanisms can be briefly understood as the reaction between the adsorbed oxygen species and acetone molecules on the active sites of sensitive materials. [24] In general, an electron depletion layer (EDL) can be formed on the near surface of $SnO_2$ nanosheets (Figure 7(a)) owing to the adsorbed oxygen species ($O^-$, $O_2^-$, and $O^{2-}$) after exposing to air and makes the absorbed oxygen species capture free electrons from the conduction band of $SnO_2$. This results in a decrease of electron concentration (or width of EDL) and thus a relatively high resistance in air atmosphere. The generation and transformation processes of the oxygen species at different operating temperatures have the following expressions [39]:

$$\begin{aligned} O_2(\text{gas}) &\longleftrightarrow O_2(\text{ads}) \\ O_2 + e^- &\longleftrightarrow O_2^- \\ O_2^- + e^- &\longleftrightarrow 2O^- \\ O^- + e^- &\longleftrightarrow O^{2-} \end{aligned} \quad (1)$$

On the contrary, upon exposure to reducing gases such as acetone, acetone molecules will react with the absorbed oxygen species, as expressed by Equation (2) and release free electrons back to the $SnO_2$ nanosheets. Hence, the electron concentration increase will cause an increase in conductivity (or a decrease in sensor resistance), and the width of EDL also becomes broader. According to the SEM and TEM observations, the vertically distributed $SnO_2$ nanosheets connect with each other to construct an interlaced electron transport network on the substrate. However, the modulation mechanism of this type of transport network is not efficient because of the same energy band structure in the pure $SnO_2$ NSAs. In other words, the $R_a$ of the pure $SnO_2$ NSA-based sensor is rather low (Figure 5(d)), which is too difficult to obtain dramatic change, especially at low acetone concentrations.

$$\begin{aligned} CH_3COCH_3 + 8O^- &\longrightarrow 3CO_2 + 3H_2O + 8e^- \\ CH_3COCH_3 + 8O^{2-} &\longrightarrow 3CO_2 + 3H_2O + 16e^- \end{aligned} \quad (2)$$

In the case of $\alpha$-$Fe_2O_3/SnO_2$ HNAs, the sensor exhibits enhanced sensitivity toward acetone, this may be attributed to the following reasons: (1) In the formation of $\alpha$-$Fe_2O_3$–$SnO_2$ n–n heterostructures, by combining these two MOXs

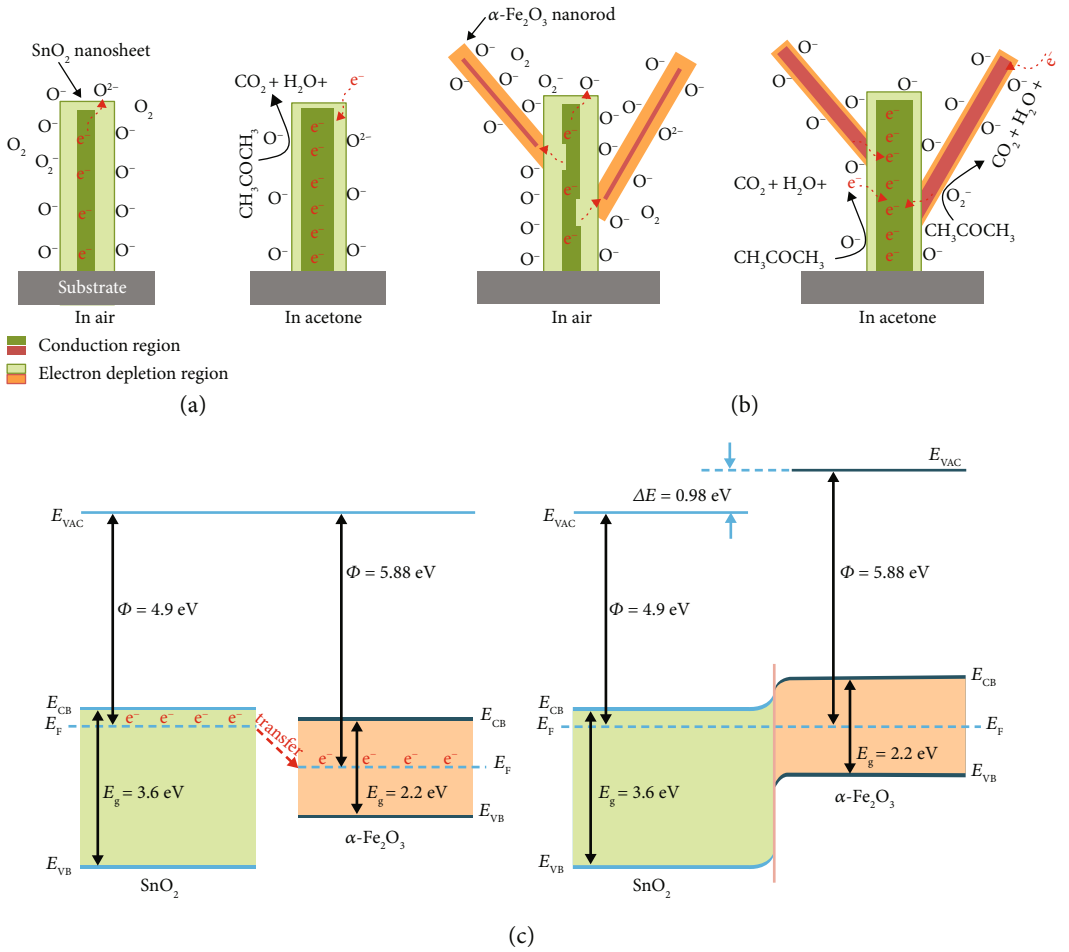


FIGURE 7: Schematic illustration of the acetone sensing mechanism of (a) the pure $SnO_2$ NSAs and (b) $\alpha$-$Fe_2O_3$/$SnO_2$ HNAs (not drawn to scale). (c) Energy band diagrams of $\alpha$-$Fe_2O_3$/$SnO_2$ system before and after equilibrium. $E_{VAC}$: the vacuum level; $E_F$: Fermi level; $E_{CB}$: the bottom of conduction band; $E_{VB}$: the top of valence band; $E_g$: band gap.

with different work functions ($SnO_2$: $\Phi = 4.9$ eV; $\alpha$-$Fe_2O_3$: $\Phi = 5.88$ eV) [40, 41], the free electrons tend to transfer from the higher side to the lower side, until the equilibrium Fermi level is reached (Figure 7(c)) [26, 42]. In this process, the $SnO_2$ nanosheet near the heterostructure interface will lose more electrons, which leads to a broader conduction region in air (Figure 7(b)) [43]. Similar to other reports, the $R_a$ of the $\alpha$-$Fe_2O_3$/$SnO_2$ HNAs in this work is much higher than that of the pure $SnO_2$ NSAs.

(2) In the novel 1D/2D $\alpha$-$Fe_2O_3$/$SnO_2$ hybrid architectures, when the sensor is exposed to acetone, the stretched-out $\alpha$-$Fe_2O_3$ NRs provide an extra surface area and active sites for the gas adsorption. Thus, more oxygen species and acetone molecules can be adsorbed on the surface of $\alpha$-$Fe_2O_3$/$SnO_2$ HNAs (Figure 7(b)), which provides more opportunities for Equation (2). The conduction region in $SnO_2$ nanosheets will be broadened as well as a decrease in $R_g$. On the other hand, the free electrons generated on the surface of $\alpha$-$Fe_2O_3$ NRs will flow to $SnO_2$ NSAs and allow a dramatic decrease in the width of the electron depletion region at the interface of the $\alpha$-$Fe_2O_3$/$SnO_2$ heterostructure. It may further result in an increase of sensor response toward acetone. So the modulation mechanism of $\alpha$-$Fe_2O_3$/$SnO_2$ HNAs becomes more efficient than that of pure $SnO_2$ NSAs. Additionally, much hard work is still needed to study the influence of ambient humidity, filter units, and clinical tests, making it more suitable for breath acetone analysis.

## 3. Conclusion

The $\alpha$-$Fe_2O_3$/$SnO_2$ HNA-based acetone sensor has been fabricated via a facile two-step on-chip growth (or CBD method) process. The results indicate that the as-prepared sensor presents a well-defined 1D/2D hybrid architecture, where the ultrathin $\alpha$-$Fe_2O_3$ NRs (an average diameter ~12.7 nm) are distributed among the interconnected $SnO_2$ NSAs. Gas sensing measurements show that the $\alpha$-$Fe_2O_3$/S-n$O_2$HNA-based sensor exhibits superior acetone sensing properties (high sensitivity, good reproducibility, and selectivity), even at a sub-ppm level, compared with those of the pure $SnO_2$ NSA- and $\alpha$-$Fe_2O_3$ NR-based sensors. The improved acetone sensing performance may be due to the formed $\alpha$-$Fe_2O_3$–$SnO_2$ heterostructures and their

unique hybrid nanostructures. Our work suggests that the $\alpha$-$Fe_2O_3$/$SnO_2$ HNAs can be a promising candidate for sub-ppm acetone detection in breath analysis.

## 4. Materials and Methods

*4.1. Preparation of $\alpha$-$Fe_2O_3$/$SnO_2$ HNAs.* In brief, 0.6 mmol $SnCl_2{\cdot}2H_2O$ and 0.8 mmol $CO(NH_2)_2$ were dissolved into 20 mL deionized water and stirred for 15 min at room temperature. Then a piece of chip with several Au electrodes was washed with acetone and ethanol and deionized water for several times, which was afterwards vertically dipped into the above solution and maintained at 95°C for 8 h. After washing and drying at 60°C in an oven, the prefabricated $SnO_2$ NSAs were immersed in an aqueous solution (containing 0.1 M $FeSO_4{\cdot}7H_2O$ and 1.0 M $CO(NH_2)_2$) and kept at 80°C for 1 h. Similarly, the chip was washed and dried again at 60°C. The final chip was annealed at 400°C for 3 h in air to achieve $\alpha$-$Fe_2O_3$/$SnO_2$ HNAs.

In addition, the pure $SnO_2$ NSAs were also annealed under the same conditions. For a pure $\alpha$-$Fe_2O_3$ NR-based sensor, 0.1 M $FeSO_4{\cdot}7H_2O$ and 1.0 M $CO(NH_2)_2$ were mixed and maintained at 80°C for 1 h, and the collected precipitate was dip-coated on the Au electrodes and then annealed at 400°C in air for 3 h.

*4.2. Characterization and Gas Sensing Measurements.* The morphologies and compositions of as-prepared products were investigated by a scanning electron microscope (SEM, Zeiss Gemini 300) equipped with energy dispersive X-ray (EDX) spectroscope and a high-resolution transmission electron microscope (HRTEM, FEI Tecnai G2 F30). The chemical states of the surface species were determined by using X-ray photoelectron spectroscopy (XPS, ESCALB 250Xi). The gas sensing properties of sensors were performed on a commercial CGS-4TPs system (Beijing Elite Tech Co., Ltd., China). Gaseous acetone diluted with dry air was injected by a syringe. The operating temperature ranges from 280 to 380°C with a relative humidity around 20%.

## Conflicts of Interest

All authors declare that there is no competing financial interest.

## Authors' Contributions

Huimin Gong, Changhui Zhao, and Fei Wang designed the experiments and contributed to the manuscript. Gaoqiang Niu and Wei Zhang carried out the material characterizations. The initial draft was edited by Changhui Zhao and Fei Wang. All authors reviewed the final version.

## Acknowledgments

The TEM characterization was performed in the Materials Characterization and Preparation Center, Southern University of Science and Technology. This work was supported in part by the Shenzhen Science and Technology Innovation Committee under Grant JCYJ20170412154426330; the Foundation for Distinguished Young Talents in Higher Education of Guangdong, China, under Grant 2018KQNX226; and Guangdong Natural Science Funds under Grants 2016A030306042 and 2018A050506001.

## Supplementary Materials

Figure S1: schematic drawing of the gas sensing measurement systems. Figure S2: SEM images of pure $\alpha$-$Fe_2O_3$ NRs. Figure S3: transient response curve of $\alpha$-$Fe_2O_3$ NRs toward different acetone concentrations at 340°C and the corresponding resistance curve. Figure S4: response/recovery time *vs.* acetone concentration (0.4-20 ppm) with $SnO_2$ NSAs and $\alpha$-$Fe_2O_3$/$SnO_2$ HNAs at 340°C. Table S1: brief summary of results reported on exhaled breath analysis. Table S2: gas sensing properties of $Fe_2O_3$–$SnO_2$ systems toward various gases. *(Supplementary Materials)*

## References

[1] C. Di Natale, R. Paolesse, E. Martinelli, and R. Capuano, "Solid-state gas sensors for breath analysis: a review," *Analytica Chimica Acta*, vol. 824, pp. 1–17, 2014.

[2] K. Schmidt and I. Podmore, "Current challenges in volatile organic compounds analysis as potential biomarkers of cancer," *Journal of Biomarkers*, vol. 2015, Article ID 981458, 16 pages, 2015.

[3] T. Arakawa, T. Suzuki, M. Tsujii et al., "Real-time monitoring of skin ethanol gas by a high-sensitivity gas phase biosensor (bio-sniffer) for the non-invasive evaluation of volatile blood compounds," *Biosensors and Bioelectronics*, vol. 129, pp. 245–253, 2019.

[4] A. T. Güntner, S. Abegg, K. Wegner, and S. E. Pratsinis, "Zeolite membranes for highly selective formaldehyde sensors," *Sensors and Actuators B: Chemical*, vol. 257, pp. 916–923, 2018.

[5] N.-H. Kim, S.-J. Choi, D.-J. Yang, J. Bae, J. Park, and I.-D. Kim, "Highly sensitive and selective hydrogen sulfide and toluene sensors using Pd functionalized $WO_3$ nanofibers for potential diagnosis of halitosis and lung cancer," *Sensors and Actuators B: Chemical*, vol. 193, pp. 574–581, 2014.

[6] M.-Y. Chuang, C.-C. Chen, H.-W. Zan, H.-F. Meng, and C.-J. Lu, "Organic gas sensor with an improved lifetime for detecting breath ammonia in hemodialysis patients," *ACS Sensors*, vol. 2, no. 12, pp. 1788–1795, 2017.

[7] I. Lee, S.-J. Choi, K.-M. Park et al., "The stability, sensitivity and response transients of ZnO, $SnO_2$ and $WO_3$ sensors under acetone, toluene and $H_2S$ environments," *Sensors and Actuators B: Chemical*, vol. 197, pp. 300–307, 2014.

[8] J. van den Broek, A. T. Güntner, and S. E. Pratsinis, "Highly selective and rapid breath isoprene sensing enabled by activated alumina filter," *ACS Sensors*, vol. 3, no. 3, pp. 677–683, 2018.

[9] E. Marco and J. O. Grimalt, "A rapid method for the chromatographic analysis of volatile organic compounds in exhaled breath of tobacco cigarette and electronic cigarette smokers," *Journal of Chromatography A*, vol. 1410, pp. 51–59, 2015.

[10] C. O. Olopade, M. Zakkar, W. I. Swedler, and I. Rubinstein, "Exhaled pentane levels in acute asthma," *Chest*, vol. 111, no. 4, pp. 862–865, 1997.

[11] Y. Xie, R. Xing, Q. Li, L. Xu, and H. Song, "Three-dimensional ordered ZnO–CuO inverse opals toward low concentration acetone detection for exhaled breath sensing," *Sensors and Actuators B: Chemical*, vol. 211, pp. 255–262, 2015.

[12] S. Liang, J. Li, F. Wang, J. Qin, X. Lai, and X. Jiang, "Highly sensitive acetone gas sensor based on ultrafine $\alpha$-$Fe_2O_3$ nanoparticles," *Sensors and Actuators B: Chemical*, vol. 238, pp. 923–927, 2017.

[13] X. Li, D. Lu, C. Shao, G. Lu, X. Li, and Y. Liu, "Hollow $CuFe_2O_4$/$\alpha$-$Fe_2O_3$ composite with ultrathin porous shell for acetone detection at ppb levels," *Sensors and Actuators B: Chemical*, vol. 258, pp. 436–446, 2018.

[14] M. Dai, L. Zhao, H. Gao et al., "Hierarchical assembly of $\alpha$-$Fe_2O_3$ nanorods on multiwall carbon nanotubes as a high-performance sensing material for gas sensors," *ACS Applied Materials & Interfaces*, vol. 9, no. 10, pp. 8919–8928, 2017.

[15] K. Wei, S. Zhao, W. Zhang et al., "Controllable synthesis of Zn-doped $\alpha$-$Fe_2O_3$ nanowires for $H_2S$ sensing," *Nanomaterials*, vol. 9, no. 7, p. 994, 2019.

[16] N. Yamazoe, "New approaches for improving semiconductor gas sensors," *Sensors and Actuators B: Chemical*, vol. 5, no. 1-4, pp. 7–19, 1991.

[17] D. R. Miller, S. A. Akbar, and P. A. Morris, "Nanoscale metal oxide-based heterojunctions for gas sensing: a review," *Sensors and Actuators B: Chemical*, vol. 204, pp. 250–272, 2014.

[18] J.-H. Lee, "Gas sensors using hierarchical and hollow oxide nanostructures: overview," *Sensors and Actuators B: Chemical*, vol. 140, no. 1, pp. 319–336, 2009.

[19] X. Li, C. Wang, H. Guo et al., "Double-shell architectures of $ZnFe_2O_4$ nanosheets on ZnO hollow spheres for high-performance gas sensors," *ACS Applied Materials & Interfaces*, vol. 7, no. 32, pp. 17811–17818, 2015.

[20] G. Niu, C. Zhao, H. Gong, Z. Yang, X. Leng, and F. Wang, "NiO nanoparticle-decorated $SnO_2$ nanosheets for ethanol sensing with enhanced moisture resistance," *Microsystems & Nanoengineering*, vol. 5, no. 1, article 21, 2019.

[21] P. Lu, W. Zhou, Y. Li, J. Wang, and P. Wu, "CuO nanosheets/ZnO nanorods synthesized by a template-free hydrothermal approach and their optical and magnetic characteristics," *Ceramics International*, vol. 43, no. 13, pp. 9798–9805, 2017.

[22] S. Park, Z. Cai, J. Lee, J. I. Yoon, and S.-P. Chang, "Fabrication of a low-concentration $H_2S$ gas sensor using CuO nanorods decorated with $Fe_2O_3$ nanoparticles," *Materials Letters*, vol. 181, pp. 231–235, 2016.

[23] P. Sun, Y. Cai, S. Du et al., "Hierarchical $\alpha$-$Fe_2O_3$/$SnO_2$ semiconductor composites: hydrothermal synthesis and gas sensing properties," *Sensors and Actuators B: Chemical*, vol. 182, pp. 336–343, 2013.

[24] Q. Yu, J. Zhu, Z. Xu, and X. Huang, "Facile synthesis of $\alpha$-$Fe_2O_3$@$SnO_2$ core–shell heterostructure nanotubes for high performance gas sensors," *Sensors and Actuators B: Chemical*, vol. 213, pp. 27–34, 2015.

[25] P. Sun, C. Wang, J. Liu et al., "Hierarchical assembly of $\alpha$-$Fe_2O_3$ nanosheets on $SnO_2$ Hollow nanospheres with enhanced ethanol sensing properties," *ACS Applied Materials & Interfaces*, vol. 7, no. 34, pp. 19119–19125, 2015.

[26] S. Yan, J. Xue, and Q. Wu, "Synchronous synthesis and sensing performance of $\alpha$-$Fe_2O_3$/$SnO_2$ nanofiber heterostructures for conductometric $C_2H_5OH$ detection," *Sensors and Actuators B: Chemical*, vol. 275, pp. 322–331, 2018.

[27] Y.-J. Chen, C.-L. Zhu, L.-J. Wang, P. Gao, M.-S. Cao, and X.-L. Shi, "Synthesis and enhanced ethanol sensing characteristics of $\alpha$-$Fe_2O_3$/$SnO_2$ core–shell nanorods," *Nanotechnology*, vol. 20, no. 4, article 045502, 2008.

[28] C. Zhao, W. Hu, Z. Zhang, J. Zhou, X. Pan, and E. Xie, "Effects of $SnO_2$ additives on nanostructure and gas-sensing properties of $\alpha$-$Fe_2O_3$ nanotubes," *Sensors and Actuators B: Chemical*, vol. 195, pp. 486–493, 2014.

[29] K. S. Choi, S. Park, and S.-P. Chang, "Enhanced ethanol sensing properties based on $SnO_2$ nanowires coated with $Fe_2O_3$ nanoparticles," *Sensors and Actuators B: Chemical*, vol. 238, pp. 871–879, 2017.

[30] P. Sun, X. Zhou, C. Wang, K. Shimanoe, G. Lu, and N. Yamazoe, "Hollow $SnO_2$/$\alpha$-$Fe_2O_3$ spheres with a double-shell structure for gas sensors," *Journal of Materials Chemistry A*, vol. 2, no. 5, pp. 1302–1308, 2014.

[31] H. Shan, C. Liu, L. Liu et al., "Excellent toluene sensing properties of $SnO_2$–$Fe_2O_3$ interconnected nanotubes," *ACS Applied Materials & Interfaces*, vol. 5, no. 13, pp. 6376–6380, 2013.

[32] L. A. Patil, M. D. Shinde, A. R. Bari, V. V. Deo, D. M. Patil, and M. P. Kaushik, "$Fe_2O_3$ modified thick films of nanostructured $SnO_2$ powder consisting of hollow microspheres synthesized from pyrolysis of ultrasonically atomized aerosol for LPG sensing," *Sensors and Actuators B: Chemical*, vol. 155, no. 1, pp. 174–182, 2011.

[33] D. D. Vuong, K. Q. Trung, N. H. Hung, N. V. Hieu, and N. D. Chien, "Facile preparation of large-scale $\alpha$-$Fe_2O_3$ nanorod/$SnO_2$ nanorod composites and their LPG-sensing properties," *Journal of Alloys and Compounds*, vol. 599, pp. 195–201, 2014.

[34] H. Gong, C. Zhao, and F. Wang, "On-chip growth of $SnO_2$/ZnO core–shell nanosheet arrays for ethanol detection," *IEEE Electron Device Letters*, vol. 39, no. 7, pp. 1065–1068, 2018.

[35] J. Shin, S.-J. Choi, I. Lee et al., "Thin-wall assembled $SnO_2$ fibers functionalized by catalytic Pt nanoparticles and their superior exhaled-breath-sensing properties for the diagnosis of diabetes," *Advanced Functional Materials*, vol. 23, no. 19, pp. 2357–2367, 2013.

[36] M.-S. Yao, W.-X. Tang, G.-E. Wang, B. Nath, and G. Xu, "MOF thin film-coated metal oxide nanowire array: significantly improved chemiresistor sensor performance," *Advanced Materials*, vol. 28, no. 26, pp. 5229–5234, 2016.

[37] W.-T. Koo, S. Yu, S.-J. Choi, J. S. Jang, J. Y. Cheong, and I. D. Kim, "Nanoscale PdO catalyst functionalized $Co_3O_4$ hollow nanocages using MOF templates for selective detection of acetone molecules in exhaled breath," *ACS Applied Materials & Interfaces*, vol. 9, no. 9, pp. 8201–8210, 2017.

[38] C. Liu, L. Zhao, B. Wang et al., "Acetone gas sensor based on NiO/ZnO hollow spheres: fast response and recovery, and low (ppb) detection limit," *Journal of Colloid and Interface Science*, vol. 495, pp. 207–215, 2017.

[39] N. Barsan and U. Weimar, "Conduction model of metal oxide gas sensors," *Journal of Electroceramics*, vol. 7, no. 3, pp. 143–167, 2001.

[40] F. Li, X. Gao, R. Wang, T. Zhang, and G. Lu, "Study on $TiO_2$-$SnO_2$ core-shell heterostructure nanofibers with different work function and its application in gas sensor," *Sensors and Actuators B: Chemical*, vol. 248, pp. 812–819, 2017.

[41] H. Xu, W. Li, R. Han et al., "Enhanced triethylamine sensing properties by fabricating Au@ $SnO_2$/$\alpha$-$Fe_2O_3$ core-shell nanoneedles directly on alumina tubes," *Sensors and Actuators B: Chemical*, vol. 262, pp. 70–78, 2018.

[42] B. Wang, X. Fu, F. Liu, S. L. Shi, J. P. Cheng, and X. B. Zhang, "Fabrication and gas sensing properties of hollow core–shell $SnO_2$/$\alpha$-$Fe_2O_3$ heterogeneous structures," *Journal of Alloys and Compounds*, vol. 587, pp. 82–89, 2014.

[43] B. Zhang, W. Fu, X. Meng, A. Ruan, P. Su, and H. Yang, "Enhanced ethanol sensing properties based on spherical-coral-like $SnO_2$ nanorods decorated with $\alpha$-$Fe_2O_3$ nanocrystallites," *Sensors and Actuators B: Chemical*, vol. 261, pp. 505–514, 2018.